Physics of the Earth and Planetary Interiors 355 (2024) 107236

Contents lists available at ScienceDirect

Physics of the Earth and Planetary Interiors

journal homepage: www.elsevier.com/locate/pepi

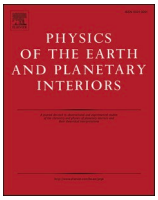

Strength, plasticity, and spin transition of Fe-N compounds in planetary cores

Allison Pease [a,*], Jiachao Liu [a], Mingda Lv [a,b], Yuming Xiao [b], Katherine Armstrong [c,d], Dmitry Popov [b], Lowell Miyagi [e], Susannah M. Dorfman [a]

[a] Department of Earth and Environmental Sciences, Michigan State University, East Lansing, MI, USA
[b] High Pressure Collaborative Access Team, X-ray Science Division, Argonne National Laboratory, Argonne, IL, USA.
[c] Lawrence Berkeley National Laboratory, Berkeley, USA
[d] Department of Earth and Planetary Sciences Department, University of California Santa Cruz, Santa Cruz, CA, USA
[e] Department of Geology and Geophysics, University of Utah, Salt Lake City, UT, USA

ARTICLE INFO

Keywords:
Fe-compounds
Nitrogen
Strength
Plasticity
Spin transitions
Diamond anvil cell

ABSTRACT

Elastic and plastic properties of Fe-light element alloys and compounds are needed to determine the compositions and dynamics of planetary cores. Elastic strength and plastic deformation mechanisms and their relationship to electronic properties of ε-Fe_7N_3 and γ'-Fe_4N mixture were investigated by x-ray diffraction and x-ray emission spectroscopy in the diamond anvil cell from 1 bar up to 60 GPa. X-ray diffraction shows that ε-Fe_7N_3 reaches a pressure of 15–20 GPa before undergoing bulk plasticity at a differential stress of 4.4–10.4 GPa. ε-Fe_7N_3 is stronger than γ'-Fe_4N and hcp-Fe which achieve a flow stress of 1.5–3.6 GPa at 10–15 GPa and 2–3 GPa at ~20 GPa, respectively. X-ray emission spectroscopy shows that a decrease in electronic spin moment begins before and completes after plastic flow onset for each nitride, suggesting that pressure-driven changes in electronic arrangement do not trigger a plastic response although they may modify the strength and plastic behavior of Fe-N compounds. Plastic deformation in ε-Fe_7N_3 and hcp-Fe results in a preferred orientation of (0001) normal to maximum compression, while γ'-Fe_4N develops a maximum in the (110). These observations may be combined with measurements of elasticity to model seismic properties of cores of small planetary bodies such as Mars, Mercury, and the Moon.

1. Introduction

The abundances of light elements such as Si, O, S, H, C, and N alloyed with Fe in planetary cores are expected to vary as a function of the composition of material accreted, accretion history, and core-mantle differentiation conditions (e.g., Poirier, 1994; Hirose et al., 2013; Litasov and Shatskiy, 2016; Lv and Liu, 2022). Nitrogen has recently been considered a potential core-forming light element due to its siderophile nature and abundance in the solar system (e.g., Minobe et al., 2015; Kusakabe et al., 2019). Evidence that iron nitrides are present in planetary building blocks and protoplanetary cores includes observations of iron nitrides in iron meteorites (Sugiura, 1998; Rubin and Ma, 2017). Diamond inclusions that may sample Earth's core-mantle boundary have also been observed to contain iron nitrides (Kaminsky and Wirth, 2017), but the abundance and distribution of nitrogen in Earth's interior have been debated (Mysen, 2019; Speelmanns et al., 2019). Even fewer observations are available to constrain the light element content within cores of other terrestrial planetary bodies, such as limited seismic observations of the cores of the Moon and Mars (Weber et al., 2011; Stähler et al., 2021) and remote sensing of density and magnetic fields (e.g. Smith et al., 2012). The cores of all of these bodies have been proposed to contain weight-percent-level carbon (Steenstra et al., 2017; Steenstra and van Westrenen, 2018; Vander Kaaden et al., 2020; Knibbe et al., 2021), although this has been controversial (Cartier and Wood, 2019; Yoshizaki and McDonough, 2020). Given the similar crystal chemical behavior of carbon and nitrogen, nitrogen may also be incorporated in iron-carbon phases in planetary cores (Minobe et al., 2015; Sagatov et al., 2019; Huang et al., 2021). To support the modeling of planetary core compositions and interpretation of future mission observations, measurements of the physical properties of iron nitrides are needed.

Multiple iron-nitrogen alloys and compounds may be stable at modest pressure conditions and low bulk nitrogen content relevant to

* Corresponding author.
E-mail address: peaseall@msu.edu (A. Pease).

https://doi.org/10.1016/j.pepi.2024.107236
Received 4 March 2024; Received in revised form 23 July 2024; Accepted 24 July 2024
Available online 27 July 2024

the interiors of small (Mars-size and smaller) terrestrial planetary cores. ε-Fe_3N_x ($0.75 < x < 1.4$, space group $P6_322$) is nonstoichiometric over a wide compositional range (on the order of 10% N or more), while stoichiometric γ'-Fe_4N (space group $Pm\bar{3}m$) forms over a narrow compositional range (within ~1% N) (Göhring et al., 2016) and typically crystallizes with excess Fe or Fe_3N_x. First principles calculations have determined that γ'-Fe_4N may be metastable under high-pressure-temperature conditions (Wetzel et al., 2021). At pressures above ~41–56 GPa and temperatures at 1000 K, both ε-Fe_3N_x and γ'-Fe_4N transition to β-Fe_7N_3 (Minobe et al., 2015; Breton et al., 2019). The ε-Fe_7N_3 to β-Fe_7N_3 transition in the Fe—N system is analogous to the hexagonal phase (h-Fe_7C_3) - orthorhombic phase (o-Fe_7C_3) transition in the iron carbide system (Prescher et al., 2015).

The similarity and miscibility of alloys in the iron-nitrogen-carbon system suggest that iron-nitrogen alloys likely exhibit similar physical properties to iron carbides that match observations of planetary cores including density, seismic wave speed, and seismic anisotropy (e.g., Deuss, 2014). Iron nitrides and carbides tend to have similar physical properties including hardness and corrosion resistance (Chen et al., 2015). Like iron carbides, iron nitrides have been predicted to be highly elastically anisotropic at 1 bar (Gressmann et al., 2007; Yang et al., 2009). Iron carbides have been proposed as constituents of Earth's core based largely on their low shear wave speed and high Poisson's ratio, unique relative to other candidate alloys in the Fe-Si, Fe-S, and Fe-H systems (Chen et al., 2014, 2018; Prescher et al., 2015). While previous studies have determined the elastic properties of iron carbides (Mookherjee, 2011; Mookherjee et al., 2011) no previous studies have measured the full elastic tensor of iron nitrides at high pressures relevant to planetary interiors. In addition to the elastic properties, mechanisms for the development of lattice-preferred orientation are important to testing whether anisotropic alloys can explain the anisotropy of planetary cores (Romanowicz and Wenk, 2017). Previous studies have measured the strength and development of lattice preferred orientation through plastic deformation of pure Fe (Miyagi et al., 2008; Merkel et al., 2013), Fe-Ni (Reagan et al., 2018), Fe-Si (Vasin et al., 2023) and Fe–Ni–Si (Brennan et al., 2021) alloys, but neither iron nitrides nor iron carbides have been studied. The preferred crystallographic orientation of elastically anisotropic ε-Fe_7N_3 and γ'-Fe_4N may produce anisotropy within small rocky bodies.

The viscoelastic behavior of iron nitrides, like other iron-light element alloys, may be modified by pressure-driven changes in electronic arrangement in iron. Magneto-elastic coupling between a transition to a low magnetic moment in *d*-orbital electrons under pressure results in significant elastic stiffening of Fe-alloys including Fe_3S, Fe_3P, Fe_3C, and Fe_7N_3 (Lv et al., 2020), softening of Fe_7C_3 (Chen et al., 2012), but no detectable effect on the equation of state of γ'-Fe_4N (Lv et al., 2020). Constraining the conditions of the electronic change in these materials via the dominant technique, X-ray emission spectroscopy (XES), is challenging due to weak signal (Rueff et al., 1999; Lin et al., 2004; Lv et al., 2020) which is sensitive to pressure gradients within the sample. Studies of electronic behavior have typically employed non-hydrostatic pressure-transmitting media, which have been observed to broaden the spin transition of ferropericlase (Lin et al., 2009) and siderite (Zhao et al., 2020). A non-hydrostatic medium may impact conclusions about the pressure ranges of the ε-Fe_7N_3 spin transition and the subsequent dependence on nitrogen content (Lv et al., 2020; Lv and Liu, 2023).

In this study, we evaluate the strengths of ε-Fe_7N_3, γ'-Fe_4N, and ε-Fe (hexagonal close-packed, or hcp) and the dependence of viscoelastic properties on pressure-induced electronic transition in ε-Fe_7N_3. The effects of non-hydrostatic stress on the electronic transition are assessed by XES applied to ε-Fe_7N_3 under compression with variable amounts of deviatoric stress in a diamond anvil cell (DAC). High-pressure strength, failure, and plastic deformation are observed using radial x-ray diffraction (XRD) on nitrides under compression with maximum deviatoric stress in a diamond anvil cell. Results are used to assess whether the preferred orientation of nitrides could occur in the cores of small terrestrial bodies such as the Moon, Mercury, and Mars.

2. Methods

The starting materials in this study are synthetic ε-Fe_7N_3 and γ'-Fe_4N powders used in Lv et al. (2020). Spotty synchrotron XRD patterns and diffraction peak widths confirm grain sizes on the order of the x-ray beam size, indicating ~2-μm grain sizes. To determine the amount of excess bcc-Fe in the γ'-Fe_4N powder starting material, quantitative phase analysis was carried out from ambient Cu-source XRD (Bruker Davinci) with full profile refinement using MAUD (Material Analysis Using Diffraction) (Lutterotti et al., 2014; Wenk et al., 2014). The unit cell parameters were $a = 3.797$ Å for γ'-Fe_4N; $a = 4.744$ Å and $c = 4.403$ Å for ε-Fe_7N_3. No excess bcc-Fe was observed in the ε-Fe_7N_3 starting material. However, in addition to γ'-Fe_4N, 11(4) at.% of the starting material was α-Fe (body-centered cubic, bcc) and 0.21(7) at.% is ε-Fe_7N_3. Observed unit cell volume of $23.53(1)$ $Å^3$ for bcc-Fe is 1% larger than values expected for pure Fe (23.27 $Å^3$, Davey, 1925), and could be explained by the volumetric expansion due to ~1% dissolved nitrogen (Lv et al., 2018).

XES measurements were conducted at beamline 16-ID-D, of the High-Pressure Collaborative Access Team (HPCAT), the Advanced Photon Source (APS), Argonne National Laboratory (ANL) in diamond anvil cells using 200- or 300-μm flat culets. A flake of ε-Fe_7N_3 was loaded into a pre-indented Be gasket with a 150- or 75-μm hole. The gasket hole was drilled at Michigan State University using an EDM (electric discharge machine) or the laser drilling system at HPCAT (Hrubiak et al., 2015). The pressure-transmitting media were cryogenically loaded Ar, solid KCl, or the sample itself with no additional medium. A 5–10 μm ruby ball was used as the pressure standard, where the pressure was determined by ruby fluorescence (Shen et al., 2020). Above the hydrostatic limit for each medium (Klotz et al., 2009; Uts et al., 2013), the reported pressure should be considered a lower bound due to the pressure gradient supported by the non-hydrostatic medium and the position of the ruby near the edge of the gasket hole. For samples without a pressure medium, the pressure was determined from the diamond edge measured using Raman spectroscopy (Akahama and Kawamura, 2006) at the GeoSoilEnviro Center for Advanced Radiation Sources (GSECARS) Raman facility. The XES measurements were performed at 300 K, up to 60 GPa, with steps of ~5 GPa. The incident x-ray energy was 11.3 keV, with a spot size of ~4 (V) by 6 (H) μm FWHM, each spectrum was recorded for 15 s/pt. with a step size of 0.4 eV. One to three spectra were collected and summed at each pressure step, accumulating at least 30,000 counts at the Fe $K\beta_{1,3}$ peak. The experimental setup is shown in Fig. 1a.

XRD measurements were conducted at beamlines 12.2.2, Advanced Light Source (ALS), Lawrence Berkeley National Lab, and 16-BM-D and 16-ID-B, APS, ANL in diamond anvil cells using 200–300-μm flat culets. A flake of ε-Fe_7N_3 or γ'-Fe_4N was loaded into a pre-indented Be or pre-polished ~50–60 μm thick boron kapton gasket (Merkel and Yagi, 2005). Beryllium gasket holes were drilled using an EDM at Michigan State University or the laser drilling system at HPCAT, APS (Hrubiak et al., 2015). Boron-epoxy gasket holes were laser drilled at 12.2.2 ALS. No pressure-transmitting medium was added to maximize non-hydrostatic stress for determining strength and plastic deformation texture. A Pt, Au, or Fe foil was placed on the sample center to mark the sample position. The XRD measurements were conducted at 300 K, up to 50 GPa, with steps of ~5 GPa. The incident x-ray wavelength was monochromatic and ranged from 30 to 42 keV, dependent on the synchrotron beamline. Diffraction is oriented perpendicular to the diamond anvil cell compression direction, as shown in Fig. 1b.

Unit cell parameters for iron nitrides at high pressure were determined in MAUD (Wenk et al., 2014) (Supplementary Table S4). A full

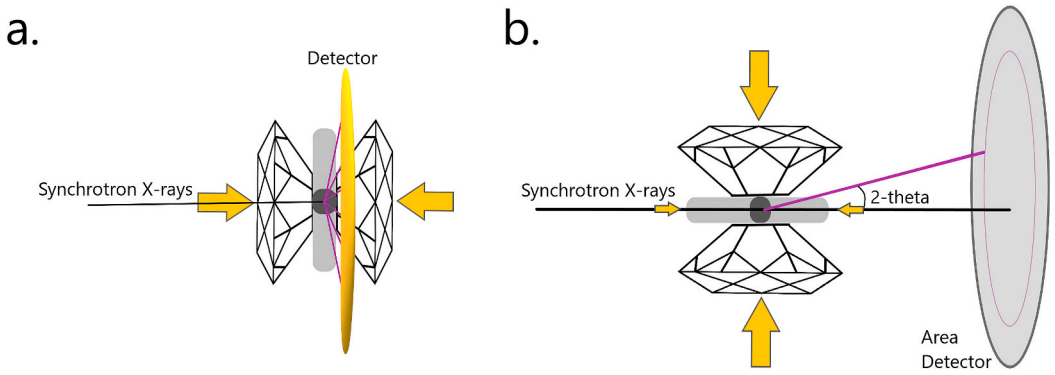

Fig. 1. Experimental setup for x-ray emission spectroscopy (XES, a) and radial x-ray diffraction (XRD, b). During an XES measurement, synchrotron x-rays enter the diamond anvil cell axially, scatter perpendicular to the x-ray beam, and are sampled by the detector. During radial XRD measurements, the synchrotron x-rays enter the diamond anvil cell radially, through the gasket, and diffract perpendicular to the direction of maximum stress.

profile refinement was used for ε-Fe_7N_3 and hcp-Fe, while individual peak fitting on (111) and (220) was used to constrain the lattice parameters of γ'-Fe_4N. The pressure was calibrated based on the equation of state for the sample (Mao et al., 1990; Lv et al., 2020) (Supplementary Table S3) for run-run consistency and to avoid overlap between sample diffraction lines and calibrants Pt and Au. For hcp-Fe, the pressure was determined by the Fe equation of state. Because the Fe exhibits some volumetric expansion probably due to N incorporation, pressure may be systematically underestimated. Nonhydrostatic stress could produce additional uncertainty in the pressure measurement through peak broadening. However, previous radial XRD experiments show good correspondence between volumes measured at the "hydrostatic angle" under non-hydrostatic compression and the hydrostatic equation of state (Duffy et al., 1999) (corresponding to the hydrostatic lattice parameters obtained from the MAUD model). For γ'-Fe_4N, lattice parameters obtained from individual diffraction peaks vary by a few GPa at the maximum pressure condition. When pressures are determined from both the ε-Fe_7N_3 sample and a Pt reference (Fei et al., 2007), the difference in pressures increases with pressure up to 6–7 GPa above 40 GPa. The absolute value of the pressure difference between the two materials can be fit as a linear function relating to pressure with a y-intercept of 0.11 and a slope of 0.14 (R^2 = 0.8), which can be used to approximate

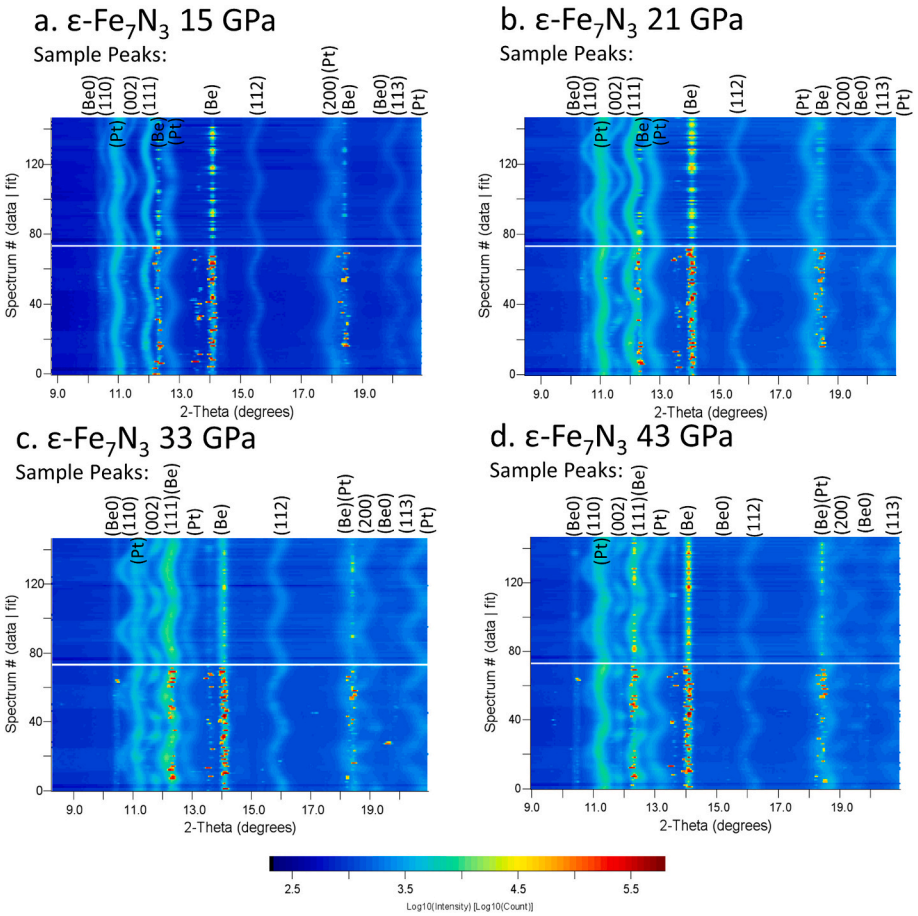

Fig. 2. 2D XRD pattern and full-profile fit carried out in MAUD for ε-Fe_7N_3 (run # c32016r1) at a) 15, b) 21, c) 33, and d) 42 GPa. The observed phases are ε-Fe_7N_3, Pt, Be (gasket), and BeO (gasket). All peaks labeled with Miller indices (hkl) correspond to ε-Fe_7N_3.

uncertainty in self-calibrated pressure for radial XRD. MAUD was also used to quantify the elastic strain on each lattice plane and determine the preferred texture orientation. In MAUD, the "*radial diffraction in the DAC*" strain model was used to fit lattice strain for each diffraction peak (Q(*hkl*)). The Orientation Distribution Function (ODF) was modeled using the *E*-WIMV model (entropy-modified Williams-Matthies-Imhof-Vinel) with a 10-degree ODF resolution and fiber symmetry.

3. Results

3.1. Stability of ε-Fe_7N_3 and γ'-Fe_4N under non-hydrostatic stress

Observed XRD peaks under non-hydrostatic stress conditions up to 50 GPa at 300 K correspond to nitrides, metallic iron, gasket, or additional markers Pt or Au (Fig. 2 and Supplementary Figs. S1 and S2). Radial XRD and full-profile refinement confirm that iron nitrides ε-Fe_7N_3 ($P6_322$) and γ'-Fe_4N ($Pm\bar{3}m$) persist at high pressures. Details of experimental conditions for each run are summarized in Supplementary Table S1. Non-hydrostatic stress does not result in amorphization or transformation of iron nitrides at 300 K. As in quasi-hydrostatic experiments by Lv et al., 2020, we assume that each iron nitride structure is metastable at the highest pressures in this study because diamond anvil cell studies with laser heating have shown that γ'-Fe_4N and ε-Fe_7N_3 transform to the beta-Fe_7N_3 phase at 56 GPa (Breton et al., 2019) and 40 GPa (Minobe et al., 2015) respectively. Because the γ'-Fe_4N starting material also contains excess α-Fe, the high-pressure radial XRD of this sample also exhibits coexisting Fe in XRD obtained in the diamond anvil cell. Bcc-Fe coexisting with γ'-Fe_4N transitioned to hcp-Fe gradually above 14 GPa. Hcp-Fe overlaps with the (200) γ'-Fe_4N peak (Supplementary Figs. S1 and S2).

3.2. Spin state of ε-Fe_7N_3 under non-hydrostatic stress

The net magnetic moment of Fe in ε-Fe_7N_3 under applied stress was determined using XES. The Fe XES spectrum is composed of a main group of peaks at 7055–7060 eV, $K_{\beta 1,3}$, and a second group of peaks at 7036–7050 eV, K'_{β}. This latter satellite peak corresponds to 3p core-hole-3d exchange interaction in a ferromagnetic high-spin state (Rueff et al., 1999). With increasing pressure, ε-Fe_7N_3 exhibits decreasing intensity of the K'_{β} peak, indicating decreasing magnetic spin moment (Fig. 3 and Supplementary Fig. S3) as previously described for iron nitrides as well as other Fe-light element alloys (Lv et al., 2020). The K'_{β} peak should decrease until it reaches a minimum that matches the low-spin state. Pyrite FeS_2 is a common reference used in other studies on Fe alloys (Rueff et al., 1999; Lin et al., 2004; Lv et al., 2020). However, at the highest pressures in all experimental runs, we observe that the K'_{β} peak falls below the intensity of the peak for FeS_2 at energies greater than ~7045–7046 eV (Fig. 3 and Supplementary Fig. S3). For the sample compressed in an Ar medium, negative relative intensity above 7046 eV is observed at the highest pressure ~ 46 GPa, while for experiments in less hydrostatic pressure-transmitting media negative relative intensity at higher energies is observed as low as ~30 GPa. This relative difference in the shape of the XES suggests that FeS_2 is not an accurate reference for the low-spin state in ε-Fe_7N_3 due either to differences in electronic structure or the stress applied to ε-Fe_7N_3. Broadening in XES spectra due to non-hydrostatic stress and pressure gradients can result in an underestimation of magnetic moment relative to the low-spin state and produce a negative apparent high spin fraction above the completion of the magnetic transition. Apparent negative spin values have also been observed in (Lin et al., 2004; Lv et al., 2020) and are likely to also be an artifact of the analysis of difference relative to standards.

The integrated relative difference (IRD) method (Mao et al., 2014) was used to quantify the net magnetic moment based on the magnitude of the K'_{β} peak relative to reference spectra. This method was used in

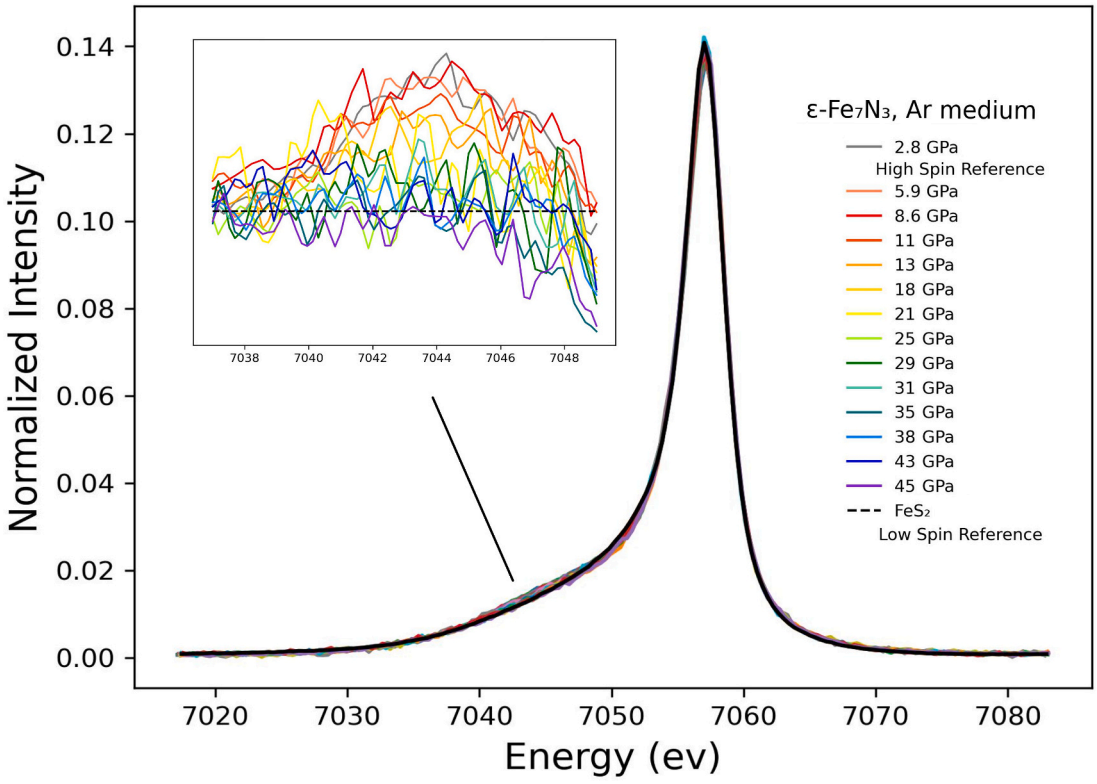

Fig. 3. Normalized XES spectra over the range of the K'_{β} peak for ε-Fe_7N_3 sample loaded with Ar. The high-spin reference is the lowest pressure measurement for each run and may represent a mixed spin state. Low-spin reference is an ambient pressure pyrite standard measured during each run.

previous studies XES of the Fe—N system (Lv et al., 2020; Lv and Liu, 2023) and is proposed to minimize the effects of nonhydrostatic stress on the analysis of the total spin moment. Each spectrum was normalized and centered about the Fe $K'_{\beta 1,3}$peak. The intensity difference between the sample and FeS_2 low-spin reference was integrated over the energy range of the K'_{β} peak from 7037 to 7050 eV. Due to the low intensity of the K'_{β} peak in alloys, it is essential to measure standards for comparison under identical beamline configuration to obtain the integrated relative difference. The high spin fraction was determined relative to the first loaded pattern collected. Because initial measurements ranged from 0 to 4 GPa depending on the sample, this initial spectrum may not be fully high spin, and calculating relative to this reference may overestimate magnetic spin moment. The IRD at low pressure thus represents an upper bound. The low spin FeS_2 reference was re-measured at ambient pressure for each experimental run.

Observations of the total spin moment for ε-Fe_7N_3 at run conditions summarized in Supplementary Table S2 are compared to reprocessed values using a silicone oil medium originally presented in Lv et al., 2020 in Fig. 4. The apparent onset of a decrease in the magnetic spin moment on compression depends on the hydrostaticity of the pressure-transmitting medium. Under quasi-hydrostatic conditions in Ar medium, ε-Fe_7N_3 remained in the high spin state until 10 GPa. In less hydrostatic KCl and silicone oil as well as samples compressed in no medium, the transition to the low spin state appears to begin at lower pressures, as soon as stress is applied. Differences in magnetic moment even at ~10 GPa when silicone oil medium is considered soft indicate that the interpretation of XES data for ε-Fe_7N_3 is sensitive to deviatoric stress.

Completion of the transition in the magnetic moment for ε-Fe_7N_3 appears delayed under non-hydrostatic stress. In an Ar medium, the data fit a sigmoid trend, with the net magnetic moment decreasing from ~10–25 GPa and completion of the transition by ~30 GPa (Fig. 4). Without a pressure-transmitting medium, the magnetic moment appears to continuously decrease and crosses 0 at ~50 GPa. We interpret apparent negative high spin fraction observations as 100% low spin. These anomalous values for the spin state are only observed when significant nonhydrostatic stress is present. We consider a hydrostatic limit given a ruby standard deviation or 0.4 this corresponds to 23 GPa for Ar medium, 11 GPa for KCl, and 9 GPa for silicone oil (Klotz et al., 2009; Uts et al., 2013). Because both nonhydrostatic stress and decreasing magnetic moment may decrease the calculated "high spin fraction," we cannot determine whether the transition is complete in highly nonhydrostatic samples with no medium or KCl medium at the maximum pressures in this study.

The pressure range of the high-to-low magnetic spin transition in ε-Fe_7N_3 is broad, taking place over ~20 GPa under quasi-hydrostatic stress. Under non-hydrostatic stress, this transition is broader. Strength and high-pressure viscoelastic deformation of ε-Fe_7N_3 must be observed by applying non-hydrostatic stress, so the effects of the magnetic transition on these deformation properties must also be assessed. Because the onset of this magnetic transition is at very low pressures and nitrides generally have high strength, elastic yielding is expected to take place after the onset of the magnetic transition.

3.3. *Strength and texture of ε-Fe_7N_3, γ'-Fe_4N, and hcp-Fe*

Radial XRD was used to determine the flow strength and texture development in ε-Fe_7N_3, γ'-Fe_4N, and hcp-Fe during high-pressure deformation (summarized in Supplementary Table S1). XRD data were collected up to 50 GPa in steps of 5 GPa. Sample diffraction peaks broaden and develop anisotropic strain as a function of orientation relative to applied non-hydrostatic stress (Fig. 2). Because the γ'-Fe_4N starting material was heterogeneous at the micron-scale of grain sizes, all experiments on γ'-Fe_4N include variable amounts of Fe co-compressed at the same conditions ranging from nearly 100% γ'-Fe_4N to nearly 80% Fe. Initial diffraction rings are smooth-spotty consistent with a randomly oriented powder. Note that the transformation of bcc-Fe to hcp-Fe resets texture and strain in this phase at ~14 GPa. For ε-Fe_7N_3, γ'-Fe_4N, and hcp-Fe, nonrandom texture development is first observed at 15–20 GPa, 10–15 GPa, and ~ 20 GPa, respectively.

The azimuthal variation of lattice spacings was fit using MAUD to obtain *Q*(*hkl*), the deviatoric lattice strain as a function of

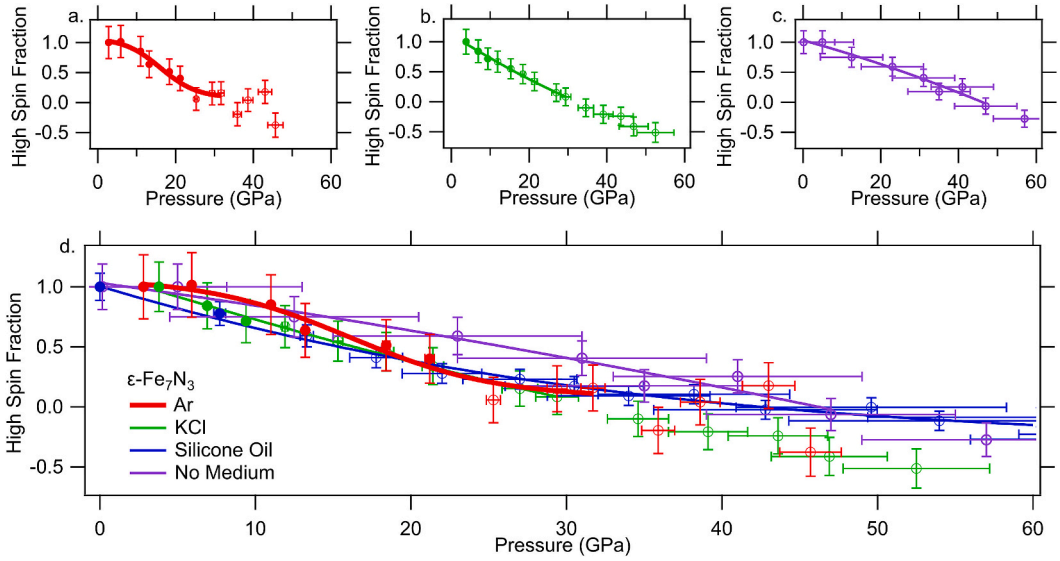

Fig. 4. High spin fraction of ε-Fe_7N_3 calculated using the IRD method with the lowest pressure point for each sample used as the high-spin reference and Fe_2S (pyrite) as low-spin reference. The transition in each dataset is fit with sigmoid curves, and all negative values have been omitted from each fit. Solid symbols represent conditions when the sample medium is believed to be quasi-hydrostatic, while open symbols are non-hydrostatic (Klotz et al., 2009; Uts et al., 2013). Red corresponds to Ar, green corresponds to KCl, blue corresponds to silicone oil, and purple corresponds to no pressure medium. The uncertainty in pressure for experiments using Ar, KCl or silicone oil media is based on the standard deviation in pressure for rubies in these media reported in previous studies (Klotz et al., 2009; Uts et al., 2013), while for experiments using no medium the pressure error bar is represented by the strength measured in this study. The uncertainty in the high spin fraction was propagated given the run-run variation of the pyrite standard. Panel a-c highlight the broadening of the spin transition with non-hydrostatic pressure media, while panel d provides run-run comparison. (For interpretation of the references to color in this figure legend, the reader is referred to the web version of this article.)

crystallographic orientation (Fig. 5, Fig. S4) (Singh et al., 1998). γ'-Fe4N and ε-Fe_7N_3 were observed to be anisotropic under compression, as indicated by the variation in $Q(hkl)$ (Supplementary Fig. S4). We identify changes in $Q(hkl)$ by visual inspection which we interpret as the the transition from elastic to elastic-plastic regimes. The range of Q for different hkl increases up to the elastic yield point, above which the anisotropy in strain remains approximately constant. At the same conditions as this change in anisotropy of strain, we also observe a change in the average $Q(hkl)$, $<Q>$, to a smaller slope of increase with pressure. For ε-Fe_7N_3, we observe a change in slope in $<Q>$ with applied pressures at ~15–20 GPa in two different runs (Fig. 5a, Supplementary Fig. S4a,b) (e.g Hemley et al., 1997). The onset of plasticity at 15–20 GPa is also supported by the development of systematic nonrandom texture above ~20 GPa (Fig. 8). For γ'-Fe_4N, the sample deformed elastically up to 10–15 GPa, after which it deformed plastically in two different runs (Fig. 5b, Supplementary Fig. S4 e,f). For hcp-Fe mixed with Fe_4N, the sample deformed elastically after the bcc-hcp transition, then above 20 GPa deformed by a combination of elastic and plastic strain (Fig. 5c, Supplementary Fig. S4 c). Yielding occurs at similar Q for different runs, with run-run differences in yield pressure up to 5–6 GPa.

Although we carried out experiments using two different gasket materials, we observed consistent results for elastic strain between runs. Strain in ε-Fe_7N_3 samples in a Be gasket is the same or higher than that in the B gasket (Fig. 5a), while, there is no significant difference between runs for γ-Fe_4N (Fig. 5b). However, when Fe is present in a greater concentration than the nitride phase we observed lower Q(hkl) values below the yield point (Fig. 5, c32021r1). Similarly, recent studies such as Perreault et al., 2022 also show that differential stress measured for strong metal tantalum is consistent for axial and radial experiments using different gasket materials, but some earlier studies (Lin et al., 2003; Miyagi et al., 2009) had suggested that observed rheology may depend on the gasket material. Miyagi et al., 2009 measured the yield stress for perovskite-structured $CaSiO_3$ compressed in a B gasket ~2× the value measured by Shieh et al., 2004 in a Be gasket, in contrast to our observations for the Fe-N system. The consistency of stress conditions in different gaskets should also depend on the strength of the sample. Because the Fe—N sample in this study is much stronger than both gaskets, it should control deformation. We note that run–run differences in stress due to changes in the shape of the sample and gasket hole also contribute to uncertainty in measurements of strain by radial XRD in the diamond anvil cell.

When deformation is purely elastic under uniaxial loading, the stress

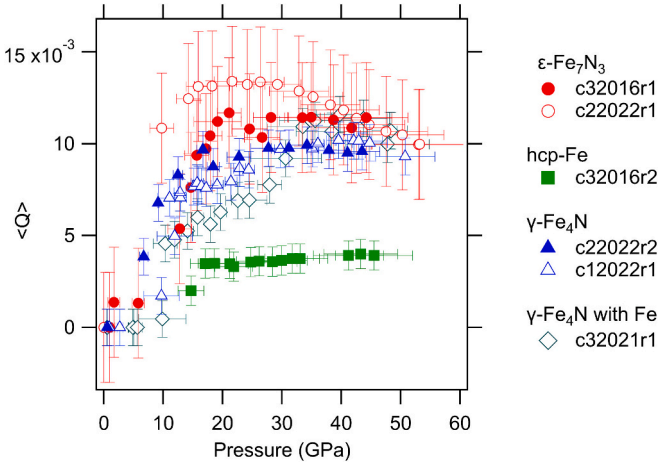

Fig. 5. Average Strain on diffraction peaks < Q > with pressure for all runs in this study. The uncertainty in < Q > is based on the average standard deviation in all Q(hkl) peaks, this corresponds to 0.003, 0.001, and 0.0008 for ε-Fe_7N_3, γ'-Fe_4N, and hcp-Fe respectively. The elastic transition point occurs at 15–20 GPa for ε-Fe_7N_3, 10–15 GPa for γ'-Fe_4N, and ~ 20 GPa for hcp-Fe.

difference between the compression axis and sample plane or differential stress, t, is limited by the strength of the sample. The average $< Q(hkl)>$, together with the shear modulus, can be used to quantify t as follows (Singh et al., 1998).

$$t = 6G_R < Q(hkl) > \quad (1)$$

Eq. 1 assumes continuity of stress across grain boundaries, allowing us to use the shear modulus defined as the Reuss average of elastic moduli, G_R.

To convert strain to stress, $G_R(P)$ is required, but there has been no high-pressure experimental measurement or theoretical prediction for the shear modulus of ε-Fe_7N_3 and γ'-Fe_4N. We estimate differential stress for ε-Fe_7N_3 and γ'-Fe_4N based on elastic constants predicted by density functional theory (DFT) using the generalized gradient approximation at 1 bar (Chen et al., 2015). We extrapolate the 1 bar shear modulus using bulk incompressibility, and an assumed range of variation in the ratio of $\frac{K}{G}$ based on the elasticity of iron and analogous iron alloys with carbon and hydrogen (Fig. 6). K_0, the 1 bar bulk modulus for each material, is fixed based on volumetric compression from Lv et al. (2020) below the spin transition onset under quasi-hydrostatic conditions. The experimental K_0 value is significantly lower than the value predicted by DFT (Fig. 6), so we fix G_{R0} based on the experimental value and the predicted 1 bar $\frac{K}{G}$ ratio from DFT. For alloys face-centered-cubic (fcc) Fe, hexagonal-close-packed (hcp) Fe, Fe_3C, Fe_7C_3 (nonmagnetic), Fe_7C_3 (magnetic), and fcc-FeH_x, published elasticity data (Söderlind et al., 1996; Steinle-Neumann et al., 1999; Crowhurst et al., 2004; Mookherjee et al., 2011; Caracas, 2015; Thompson et al., 2018) indicate that $\frac{K}{G}$ is constant or changes slightly with pressure up to 50 GPa with a slope of −0.007–0.013 GPa^{-1}. Using this range as an envelope for $\frac{K}{G}$ for each iron nitride, the range of expected values for G_R is shown in Fig. 6. At 15–20 GPa, for ε-Fe_7N_3, we estimate G_R between 94 and 131 GPa, corresponding to a strength of 4.4–10.4 GPa. For γ'-Fe_4N at 10–15 GPa, G_R could be 47–80 GPa, and strength is estimated to be 1.5–3.6 GPa (Fig. 7).

Texture development in ε-Fe_7N_3, γ'-Fe_4N, and hcp-Fe is a result of slip and twin activity during deformation at extreme pressure. Significant texture development is expected to begin at pressures above the change in slope of elastic strain $Q(hkl)$ with pressure. In each of the experiments on ε-Fe_7N_3, during compression, a maximum develops near (0001) in the inverse pole figure (IPF). At high pressure, a weaker secondary maximum develops at $(01\bar{1}0)$ and by 42 GPa at $(11\bar{2}0)$ in the IPF (Fig. 8). Alignment of (0001) planes at high angle to compression with a secondary maximum at $(11\bar{2}0)$ is consistent with basal slip for hexagonal metals (e.g. Miyagi et al., 2008). Due to the overlap between γ'-Fe_4N and hcp-Fe, lattice-preferred orientation could only be obtained from a single diffraction line, (111). For this phase texture is characterized by the alignment of {110} at high angles to compression. This is a typical compression texture for fcc structure and is attributed to dominant slip on $\{111\}\langle 110\rangle$ (e.g. (Miyagi et al., 2008)). Lattice preferred orientation in hcp-Fe is consistent with previous studies conducted on hcp-Fe that report (0001) maximum (Merkel et al., 2004, 2013). The (0001) maximum might be the result of basal slip and/or tensile $\{10\bar{1}2\}<\bar{1}011>$ twinning (Miyagi et al., 2008), confirming that co-compression with γ'-Fe_4N and possible up to ~1% N impurity in the metallic Fe do not significantly impact the deformation texture of hcp-Fe.

4. Discussion

During a magnetic transition, the transition is a mechanism for accommodating deformation and is typically expected to result in elastic softening relative to pre- or post-transition states. Under non-hydrostatic stress, magnetic transitions in ε-Fe_7N_3 began below the flow stress of 15–20 GPa. The magnetic transition initiates as the Fe-nitrides deform elastically and do not immediately trigger flow. Under hydrostatic stress, ε-Fe_7N_3 remains in the high spin state until at least 10 GPa. Previous experiments (Lv et al., 2020) observed the onset of the

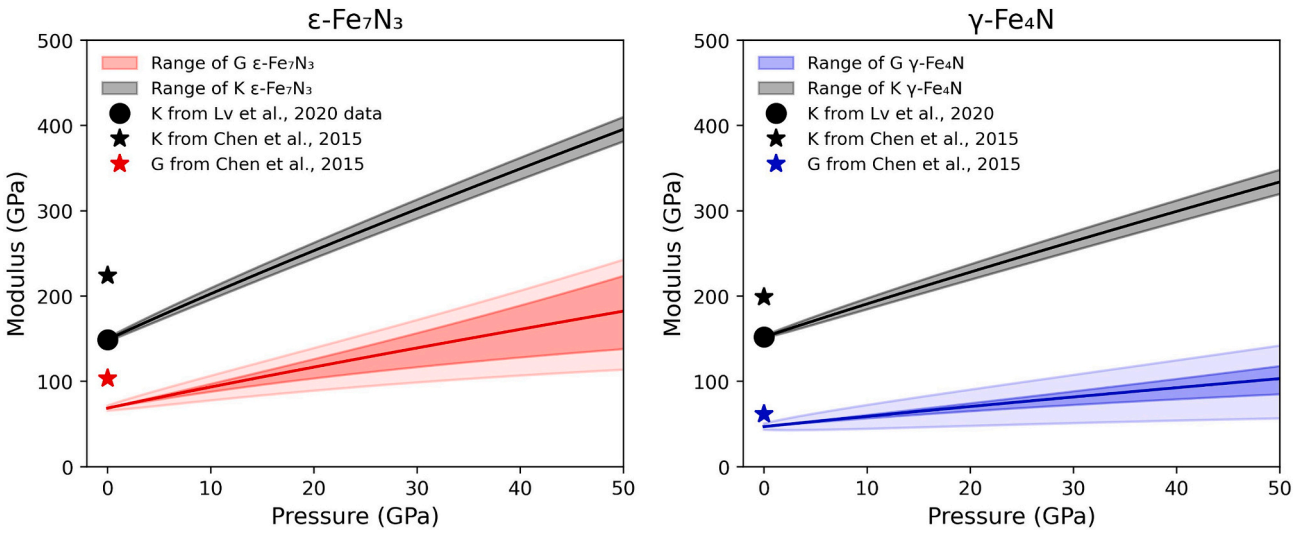

Fig. 6. Published data on G and K for ε-Fe_7N_3 and γ'-Fe_4N extrapolated to high pressure. K_0, the 1 bar bulk modulus for each material, is fixed based on volumetric compression from Lv et al. (2020), values in Supplementary Table S3. The 1 bar $\frac{K}{G}$ ratio from (Chen et al., 2015) was used to determine G_0 and extrapolate to higher pressures, to determine the differential stress of each material.

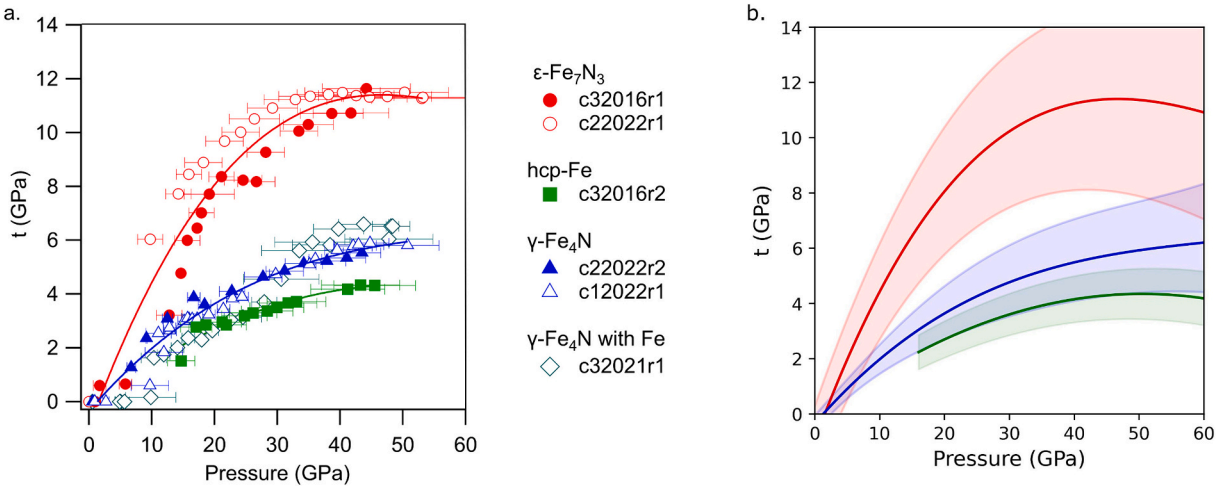

Fig. 7. a) Differential stress for all runs for each Fe-nitride. b) uncertainty in differential stress for iron and iron nitrides associated with the uncertainty in <Q > and the approximation of G_R. Solid lines are 4th order polynomial fits to ε-Fe_7N_3, γ'-Fe_4N *and a 3rd order polynomial fit to hcp-Fe.*

magnetic transition at lower pressures, 10 GPa for ε-Fe_7N_3 and 5 GPa for γ'-Fe_4N, due to different stress conditions in the silicone oil pressure transmitting medium. Because no first or second-order discontinuity was observed in the equation of state of either material at these conditions, no difference could be distinguished between elastic properties of a high spin state relative to a mixed spin state for either ε-Fe_7N_3 or γ'-Fe_4N (Lv et al., 2020). With a revision of the spin transition onset to higher pressures, the lack of an effect of the onset of the transition on bulk compressibility remains robust. However, to accurately determine the equation of state for nitrides in high, mixed, and low spin states, the spin transition conditions observed in a quasi-hydrostatic medium should be used to determine the pressure ranges for these electronic configurations. The updated 3rd-order Birch-Murnaghan equation of state parameters obtained for high and mixed spin/magnetic ε-Fe_7N_3 and low spin/nonmagnetic ε-Fe_7N_3 are listed in Supplementary Table S3.

The completion pressures of magnetic transitions in ε-Fe_7N_3 under non-hydrostatic stress are higher than the pressures of flow. Different stress conditions affect the breadth of the spin transition. Relative to the samples compressed in a quasi-hydrostatic Ar medium, samples compressed with no medium are observed to undergo the transition over 10s of GPa. Given that the maximum pressure of radial diffraction measurements in this study is around 50 GPa, we cannot assess whether a change in deformation texture or effective strength takes place after the magnetic transition. Previous work identified a stiffening in elastic incompressibility for ε-Fe_7N_3 as well as Fe_3S, Fe_3P, and Fe_3C (Lv et al., 2020). In this study and previous studies (Lin et al., 2009; Zhao et al., 2020), non-hydrostatic pressure media have been observed to broaden spin transitions in multiple materials. The experimental conditions used may impact the interpretation of the effects of magnetic transitions on the incompressibility of materials, especially Fe alloys.

Whether the magnetic moment of electrons in iron alloys has a significant effect on observable density and seismic wave speeds of planetary cores also depends on the conditions of electronic transitions relative to planetary interiors. Throughout the Earth's core, iron nitrides may be inferred to adopt a low spin configuration unless the extreme high temperatures of the core promote mixed excited states. The spin transition for iron nitrides observed in this study (1 bar to ~50 GPa) at 300 K corresponds to the pressures found in the mantle and core of Mars (~1–40 GPa), the moon (~1–6 GPa), and Mercury (~1–40 GPa) (Trønnes et al., 2019). At planetary interior temperatures, electronic

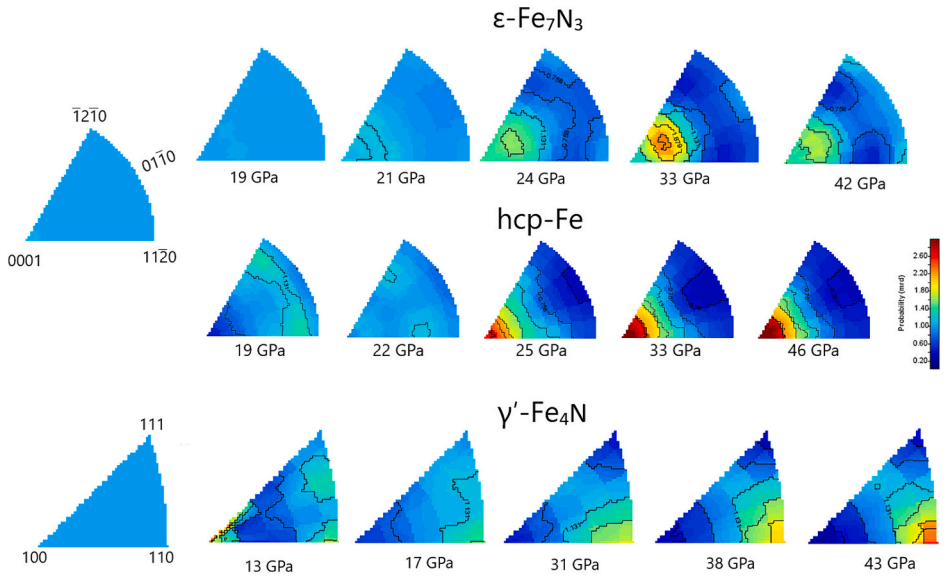

Fig. 8. Inverse pole figures of the compression direction for iron–nitrogen compounds corresponding to the orientation normal to the maximum stress. Texture development in ε-Fe_7N_3 (run # c32016r1) developed a maximum near (0001). Texture development in hcp-Fe (run # c32016r2) developed a maximum near (0001). Texture development in γ'-Fe_4N (run # c22022r2) developed a maximum near (110). All plots are scaled to a common color bar in multiples of random distribution (mrd).

transitions will be broadened, resulting in a more gradual change in properties. For example, temperature broadens the spin transition in ferropericlase from a 45–65 GPa range at 300 K to a 60–100 GPa range at 1700 K (Komabayashi et al., 2010). We expect that, in the iron nitride system, extreme temperatures will also broaden the spin transition making it even more difficult to observe a change in density or seismic wave speed.

In addition, Lv et al., 2020's data on each nitride demonstrated that the bulk moduli of γ'-Fe_4N do not change significantly during the spin transition, while for ε-Fe_7N_3 the change is slight. While there is no constraint on the shear modulus with pressure during the transition for a magnetic and non-magnetic phase of each iron nitride, studies on Fe_7C_3, an analog system for the high-pressure iron nitride beta phase due to the formation of a solid solution (Minobe et al., 2015; Kusakabe et al., 2019), indicate that the biggest effect of the spin transition on mechanical properties may be seen in the shear modulus. Calculations of

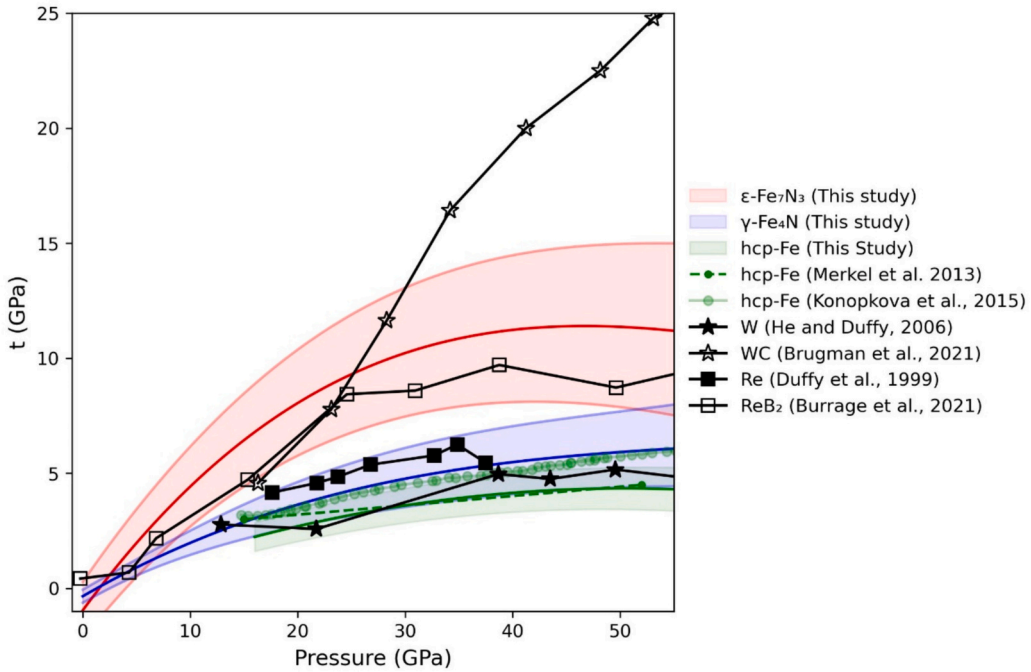

Fig. 9. Differential stress measured at high pressures for metals and alloys under static compression at 300 K (this study, (Duffy et al., 1999; He and Duffy, 2006; Brugman et al., 2021; Burrage et al., 2021)) and dynamic (10^{-2} s^{-1}) diamond anvil cell compression at 300 K (Konôpková et al., 2015). The differential stress increases with light element abundance for Fe (green circles), W (black stars), and Re (black squares). Light elements bearing alloy symbols are open, while pure elements (<1 wt% light element) are represented by closed symbols. The error bars (red and blue) in this study account for the possible range in G based on the of $\frac{K}{G}$ extrapolation. (For interpretation of the references to color in this figure legend, the reader is referred to the web version of this article.)

the change in the shear and bulk modulus with pressure for a magnetic and nonmagnetic phase (Mookherjee et al., 2011) find that the spin transition for Fe_7C_3 results in changes in the bulk modulus by approximately 10% and the shear modulus by approximately 20%. The softening of elastic constants is significant in Fe_7C_3 and may indicate softening in the iron nitride system. The magnitude of the change in the shear modulus will determine if the spin transition significantly affects the elastic properties of planetary cores.

The incorporation of light elements in metals has been well-known over the history of metallurgy to result in higher hardness, elastic moduli, and strength. In this study, we demonstrate that ε-Fe_7N_3 and γ'-Fe_4N are stronger than hcp-Fe under compression (Fig. 9). This is in line with previous studies that have shown that, at ambient conditions, metal-light element alloys and compounds are stronger at high pressure than pure metals (Duffy et al., 1999; He and Duffy, 2006; Brugman et al., 2021; Burrage et al., 2021). The combination of covalent and metallic bonds strengthens alloys and compounds between metals Fe, W, and Re and light elements N, C, or B (Fig. 9). While this study investigates Fe and Fe—N compounds a similar trend can be observed in Fe-alloys that may be found within planetary cores. For example, previous studies on Fe—Si alloys observe that increasing Si content increases the strength of hcp-Fe (Brennan et al., 2021). The differential stress observed in Fe—Si alloys (with 9 wt% Si) is around 4–6 GPa at pressures >30 GPa (Kolesnikov et al., 2022; Vasin et al., 2023). These Fe—Si alloys exhibit similar differential stresses to our γ'-Fe_4N experiments but are lower than ε-Fe_7N_3.

Our observed strength of metallic Fe (possibly containing ~1% N) is similar to the strength of pure Fe measured under quasi-static diamond anvil cell compression (Miyagi et al., 2008; Merkel et al., 2013) and systematically lower than values obtained using dynamic membrane-driven diamond anvil cell compression (Konôpková et al., 2015) below 50 GPa or shock compression (Ping et al., 2013) above 50 GPa (Fig. 9). Typical strain rates during quasi-static diamond anvil cell compression experiments such as those of Merkel et al., 2013 are on the order of 10^{-5}–10^{-4} s^{-1}, while the fast compression of Konôpková et al., 2015 was carried out at a reported strain rate of 10^{-2} s^{-1}. Dynamic strength observed under rapid strain is generally higher than static strength under gradual compression (Fig. 9). Inner core deformation has been suggested to take place over a range of strain rates from as low as 10^{-18} due to slow core crystallization to as high as 10^{-9} s^{-1} due to buoyancy and Maxwell stresses (e.g Sumita and Bergman, 2007). These rates are outside the conditions observed in static and dynamic compression experiments. Higher strain rates observed in fast compression are relevant to planetary impacts but might not represent the strain rates in the inner core. The dependence of the strengths of Fe and Fe alloys on strain rate is thus important for modeling a range of processes in planetary cores.

5. Conclusions

The conditions of the magnetic transitions in iron nitrides have been determined to reassess the coupling between magnetic and elastic behavior. The spin transition is complete for ε-Fe_7N_3 at ~30 GPa under (quasi) hydrostatic stress. Under more non-hydrostatic stress, the spin transition is observed over a broader range of pressures. The difference in spin transition condition impacts the pressure range of data used to determine the equation of state of iron nitrides in magnetic and non-magnetic states, and revised equations of state are presented for high/mixed-spin and low-spin ε-Fe_7N_3. Spin transitions may be expected to be further broadened at temperatures relevant to planetary interiors (Lin et al., 2013). Due to the low pressures of the cores of the Moon, Mars, and Mercury relative to the spin transition completion pressure, if Fe-nitrides are present, they are likely to adopt a mixed spin state.

By approximating the shear moduli of iron nitrides G_R, we determine strength to range from 4.4 to 10.4 GPa for ε-Fe_7N_3 and 1.5–3.6 GPa for γ'-Fe_4N. This is consistent with Vickers hardness measurements and calculations that indicate that ε-Fe_3N_x has a hardness of 9.48 GPa (Chen et al., 2015), while γ'-Fe_4N is slightly softer at 6.01 GPa (Chen et al., 2015). Strength increases with N content, with Fe being the weakest and ε-Fe_7N_3 being the strongest. The combination of metallic and covalent bonds strengthens Fe, as with other metals such as Re and W. The higher strength of iron-nitrogen compounds relative to pure iron at pressures found within the cores of small terrestrial bodies such as Mars, Mercury, and the Moon results in greater differential stresses needed to induce yielding and lattice-preferred orientation relative to pure Fe.

Texture development for γ'-Fe_4N results in (110) at a high angle to compression, while Fe and ε-Fe_7N_3 develop (0001) maxima in the IPF. This lattice-preferred orientation persists with pressure for γ'-Fe_4N and hcp-Fe. Above 30 GPa, ε-Fe_7N_3 gradually developed a secondary maximum near $(01\bar{1}0)$ and finally $(11\bar{2}0)$. Based on the elasticity of ε-Fe_7N_3 and γ'-Fe_4N computed at 1 bar in previous work, this alignment may result in anisotropic seismic wave speeds, but additional research is needed to determine elastic anisotropy at planetary conditions. As suggested by others (e.g Romanowicz and Wenk, 2017; Frost et al., 2021) the development of lattice-preferred orientation at high differential stress conditions can facilitate seismic anisotropy within planetary interiors.

Seismic waves within the Earth's core have been observed to match the low shear wave velocities and high Poisson ratios of iron carbides (Chen et al., 2014, 2018; Prescher et al., 2015). Recently, experimental studies have demonstrated that nitrogen can alloy with iron carbides (Minobe et al., 2015). If carbides or nitrides are present within planetary cores, they will coexist with a dominant Fe—Ni alloy. This study has constrained the behavior of iron and iron-nitride mixtures, providing essential support for modeling planetary core composition and informing interpretations of future missions. Future missions that place seismometers on terrestrial bodies are needed to resolve outstanding questions about the light element content of planetary cores and the distribution of volatile light elements in the solar system.

CRediT authorship contribution statement

Allison Pease: Writing – review & editing, Writing – original draft, Investigation, Formal analysis, Data curation, Conceptualization. **Jiachao Liu:** Investigation, Data curation, Conceptualization. **Mingda Lv:** Investigation, Data curation, Conceptualization. **Yuming Xiao:** Writing – review & editing, Resources, Data curation. **Katherine Armstrong:** Writing – review & editing, Investigation, Data curation. **Dmitry Popov:** Resources, Data curation. **Lowell Miyagi:** Writing – review & editing, Resources. **Susannah M. Dorfman:** Writing – review & editing, Writing – original draft, Resources, Investigation, Funding acquisition, Data curation, Conceptualization.

Declaration of competing interest

The authors declare the following financial interests/personal relationships which may be considered as potential competing interests:

Susannah Dorfman, Mingda Lv, Lowell Miyagi reports financial support was provided by National Science Foundation. Allison Pease reports financial support, equipment, drugs, or supplies, and travel were provided by National Nuclear Security Administration. Allison Pease, Jiachao Liu, Mingda Lv, Yuming Xiao, Katherine Armstrong, Dmitry Popov, Lowell Miyagi, and Susannah M. Dorfman reports equipment, drugs, or supplies was provided by Department of Energy. We have a COI with Jie Li editor of PEPI. Jie Li was the graduate supervisor to corresponding author A. Pease and coauthor J. Liu and has an ongoing grant with S. Dorfman. If there are other authors, they declare that they have no known competing financial interests or personal relationships that could have appeared to influence the work reported in this paper.

Data availability

Data will be made available on request.

Acknowledgments

We would like to acknowledge the assistance provided by B. Brugman, S. Chariton, L. Chavarría, H. Krauss, M. Kunz, E. Ledoux, Y. Meng, C. Park, V. Prakapenka, R. Staples, N. Singleton, H. Wang at Argonne National Laboratory, Lawrence Berkeley National Laboratory, and/or Michigan State University. We would also like to acknowledge J. Li for supplying additional starting material. Ambient XRD was carried out at the MSU Center for Crystallographic Research. A. Pease and beamline facility access was supported by the US Department of Energy, National Nuclear Security Administration, through the Chicago/DOE Alliance Center (DE-NA0003975). S. Dorfman and M. Lv acknowledge support from NSF EAR-1751664. L. Miyagi acknowledges support from NSF EAR-2054993. Support for the participation of N. Singleton was provided by the GeoCaFES program, NSF Geopaths grant 2023059. Beamline 12.2.2 at the Advanced Light Source is a DOE Office of Science User Facility under contract no. DE-AC02-05CH11231. This research was partially supported by COMPRES, the Consortium for Materials Properties Research in Earth Sciences under NSF Cooperative Agreement EAR 1606856. Portions of this work were performed at HPCAT (Sector 16) and GSECARS (Sector 13), Advanced Photon Source (APS), Argonne National Laboratory. HPCAT operations are supported by DOE-NNSA's Office of Experimental Sciences. The Advanced Photon Source, a U.S. Department of Energy (DOE) Office of Science User Facility operated for the DOE Office of Science by Argonne National Laboratory under Contract No. DE-AC02-06CH11357. Use of the GSECARS Raman Lab System was supported by the NSF MRI Proposal (EAR-1531583).

Appendix A. Supplementary data

Supplementary data to this article can be found online at https://doi.org/10.1016/j.pepi.2024.107236.

References

Akahama, Y., Kawamura, H., 2006. Pressure calibration of diamond anvil Raman gauge to 310GPa. J. Appl. Phys. 100, 43516.
Brennan, M.C., Fischer, R.A., Couper, S., Miyagi, L., Antonangeli, D., Morard, G., 2021. High-pressure deformation of Iron–nickel–silicon alloys and implications for Earth's inner core. J. Geophys. Res. Solid Earth 126, e2020JB021077.
Breton, H., Komabayashi, T., Thompson, S., Potts, N., McGuire, C., Suehiro, S., Anzellini, S., Ohishi, Y., 2019. Static compression of Fe4N to 77 GPa and its implications for nitrogen storage in the deep earth. Am. Mineral. 104, 1781–1787.
Brugman, B.L., Lin, F., Lv, M., Kenney-Benson, C., Popov, D., Miyagi, L., Dorfman, S.M., 2021. Strength, deformation, and equation of state of tungsten carbide to 66 GPa. Acta Mater. 220, 117301.
Burrage, K.C., Park, C., Vohra, Y.K., 2021. Shear strength measurements and hydrostatic compression of rhenium diboride under high pressures. J. Appl. Phys. 129, 205901.
Caracas, R., 2015. The influence of hydrogen on the seismic properties of solid iron. Geophys. Res. Lett. 42, 3780–3785.
Cartier, C., Wood, B.J., 2019. The role of reducing conditions in building mercury. Elements 15, 39–45.
Chen, B., Gao, L., Lavina, B., Dera, P., Alp, E.E., Zhao, J., Li, J., 2012. Magneto-elastic coupling in compressed Fe7C3 supports carbon in Earth's inner core. Geophys. Res. Lett. 39.
Chen, B., Li, Z., Zhang, D., Liu, J., Hu, M.Y., Zhao, J., Bi, W., Alp, E.E., Xiao, Y., Chow, P., et al., 2014. Hidden carbon in Earth's inner core revealed by shear softening in dense Fe7C3. Proc. Natl. Acad. Sci. 111, 17755–17758.
Chen, B., Lai, X., Li, J., Liu, J., Zhao, J., Bi, W., Ercan Alp, E., Hu, M.Y., Xiao, Y., 2018. Experimental constraints on the sound velocities of cementite Fe3C to core pressures. Earth Planet. Sci. Lett. 494, 164–171.
Chen, J.S., Yu, C., Lu, H., 2015. Phase stability, magnetism, elastic properties and hardness of binary iron nitrides from first principles. J. Alloys Compd. 625, 224–230.
Crowhurst, J.C., Goncharov, A.F., Zaug, J.M., 2004. Impulsive stimulated light scattering from opaque materials at high pressure. J. Phys. Condens. Matter 16, S1137.
Davey, W.P., 1925. Precision measurements of the lattice constants of twelve common metals. Phys. Rev. 25, 753–761.
Deuss, A., 2014. Heterogeneity and anisotropy of Earth's inner Core. Annu. Rev. Earth Planet. Sci. 42, 103–126.
Duffy, T.S., Shen, G., Heinz, D.L., Shu, J., Ma, Y., Mao, H.-K., Hemley, R.J., Singh, A.K., 1999. Lattice strains in gold and rhenium under nonhydrostatic compression to 37 GPa. Phys. Rev. B 60, 15063–15073.
Fei, Y., Ricolleau, A., Frank, M., Mibe, K., Shen, G., Prakapenka, V., 2007. Toward an internally consistent pressure scale. Proc. Natl. Acad. Sci. 104, 9182–9186.
Frost, D.A., Lasbleis, M., Chandler, B., Romanowicz, B., 2021. Dynamic history of the inner core constrained by seismic anisotropy. Nat. Geosci. 14, 531–535.
Göhring, H., Fabrichnaya, O., Leineweber, A., Mittemeijer, E.J., 2016. Thermodynamics of the Fe-N and Fe-N-C systems: the Fe-N and Fe-N-C phase diagrams revisited. Metall. Mater. Trans. A 47, 6173–6186.
Gressmann, T., Wohlschlögel, M., Shang, S., Welzel, U., Leineweber, A., Mittemeijer, E.J., Liu, Z.-K., 2007. Elastic anisotropy of γ'-Fe4N and elastic grain interaction in γ'-Fe4N1−y layers on α-Fe: first-principles calculations and diffraction stress measurements. Acta Mater. 55, 5833–5843.
He, D., Duffy, T.S., 2006. X-ray diffraction study of the static strength of tungsten to 69 GPa. Phys. Rev. B 73, 134106.
Hemley, R.J., Mao, H., Shen, G., Badro, J., Gillet, P., Hanfland, M., Häusermann, D., 1997. X-ray imaging of stress and strain of diamond, Iron, and tungsten at Megabar pressures. Science 276, 1242–1245.
Hirose, K., Labrosse, S., Hernlund, J., 2013. Composition and state of the core. Annu. Rev. Earth Planet. Sci. 41, 657–691.
Hrubiak, R., Sinogeikin, S., Rod, E., Shen, G., 2015. The laser micro-machining system for diamond anvil cell experiments and general precision machining applications at the high pressure collaborative access team. Rev. Sci. Instrum. 86.
Huang, S., Wu, X., Zhu, F., Lai, X., Li, J., Neill, O.K., Qin, S., Rapp, R., Zhang, D., Dera, P., et al., 2021. High-pressure phase stability and thermoelastic properties of Iron Carbonitrides and nitrogen in the deep earth. J. Geophys. Res. Solid Earth 126, e2021JB021934.
Kaminsky, F., Wirth, R., 2017. Nitrides and carbonitrides from the lowermost mantle and their importance in the search for Earth's "lost" nitrogen. Am. Mineral. 102, 1667–1676.
Klotz, S., Chervin, J.-C., Munsch, P., Le Marchand, G., 2009. Hydrostatic limits of 11 pressure transmitting media. J. Phys. D. Appl. Phys. 42, 75413.
Knibbe, J.S., Rivoldini, A., Luginbuhl, S.M., Namur, O., Charlier, B., Mezouar, M., Sifre, D., Berndt, J., Kono, Y., Neuville, D.R., et al., 2021. Mercury's interior structure constrained by density and P-wave velocity measurements of liquid Fe-Si-C alloys. J. Geophys. Res.: Planets 126, e2020JE006651.
Kolesnikov, E., Kupenko, I., Achorner, M., Plückthun, C., Liermann, H.-P., Merkel, S., Sanchez-Valle, C., 2022. Strength and seismic anisotropy of textured FeSi at planetary core conditions. Front. Earth Sci. 10.
Komabayashi, T., Hirose, K., Nagaya, Y., Sugimura, E., Ohishi, Y., 2010. High-temperature compression of ferropericlase and the effect of temperature on iron spin transition. Earth Planet. Sci. Lett. 297, 691–699.
Konôpková, Z., Rothkirch, A., Singh, A.K., Speziale, S., Liermann, H.-P., 2015. In situ x-ray diffraction of fast compressed iron: analysis of strains and stress under non-hydrostatic pressure. Phys. Rev. B 91, 144101.
Kusakabe, M., Hirose, K., Sinmyo, R., Kuwayama, Y., Ohishi, Y., Helffrich, G., 2019. Melting Curve and Equation of State of β-Fe 7 N 3 : Nitrogen in the Core? J. Geophys. Res.: Solid Earth. 124, 3448–3457.
Lin, J.-F., Shu, J., Mao, H., Hemley, R.J., Shen, G., 2003. Amorphous boron gasket in diamond anvil cell research. Rev. Sci. Instrum. 74, 4732–4736.
Lin, J.-F., Struzhkin, V.V., Mao, H., Hemley, R.J., Chow, P., Hu, M.Y., Li, J., 2004. Magnetic transition in compressed Fe3C from x-ray emission spectroscopy. Phys. Rev. B 70, 212405.
Lin, J.-F., Wenk, H.-R., Voltolini, M., Speziale, S., Shu, J., Duffy, T.S., 2009. Deformation of lower-mantle ferropericlase (Mg,Fe)O across the electronic spin transition. Phys. Chem. Miner. 36, 585.
Lin, J.-F., Speziale, S., Mao, Z., Marquardt, H., 2013. Effects of the electronic spin transitions of iron in lower mantle minerals: implications for deep mantle geophysics and geochemistry. Rev. Geophys. 51, 244–275.
Litasov, K.D., Shatskiy, A.F., 2016. Composition of the Earth's core: a review. Russ. Geol. Geophys. 57, 22–46.
Lutterotti, L., Vasin, R., Wenk, H.-R., 2014. Rietveld texture analysis from synchrotron diffraction images. I. Calibration and basic analysis. Powder Diffract. 29, 76–84.
Lv, C., Liu, J., 2022. Early planetary processes and light elements in iron-dominated cores. Acta Geochim. 41, 625–649.
Lv, C., Liu, J., 2023. The iron spin transition of deep nitrogen-bearing mineral Fe3N1.2 at high pressure, 108, 653–658.
Lv, M., Liu, J., Zhu, F., Li, J., Zhang, D., Xiao, Y., Dorfman, S.M., 2020. Spin transitions and compressibility of ε-Fe7N3 and γ'-Fe4N: implications for Iron alloys in terrestrial planet cores. J. Geophys. Res. Solid Earth 125, 1–15.
Lv, Z., Fan, J., Guan, K., Wu, Z., Zhao, D., Fu, W., 2018. Effects of interstitial atoms (N/O) in bcc Fe from first-principle calculations. Fusion Eng. Des. 137, 22–29.
Mao, H.K., Wu, Y., Chen, L.C., Shu, J.F., Jephcoat, A.P., 1990. Static compression of iron to 300 GPa and Fe0.8Ni0.2 alloy to 260 GPa: implications for composition of the core. J. Geophys. Res. Solid Earth 95, 21737–21742.
Mao, Z., Lin, J.F., Yang, J., Wu, J., Watson, H.C., Xiao, Y., Chow, P., Zhao, J., 2014. Spin and valence states of iron in Al-bearing silicate glass at high pressures studied by synchrotron Mössbauer and X-ray emission spectroscopy. Am. Mineral. 99, 415–423.
Merkel, S., Yagi, T., 2005. X-ray transparent gasket for diamond anvil cell high pressure experiments. Rev. Sci. Instrum. 76, 46109.
Merkel, S., Wenk, H.-R., Gillet, P., Mao, H., Hemley, R.J., 2004. Deformation of polycrystalline iron up to 30GPa and 1000K. Phys. Earth Planet. Inter. 145, 239–251.

Merkel, S., Liermann, H.-P., Miyagi, L., Wenk, H.-R., 2013. In situ radial X-ray diffraction study of texture and stress during phase transformations in bcc-, fcc- and hcp-iron up to 36GPa and 1000K. Acta Mater. 61, 5144–5151.
Minobe, S., Nakajima, Y., Hirose, K., Ohishi, Y., 2015. Stability and compressibility of a new iron-nitride β-Fe 7 N 3 to core pressures. Geophys. Res. Lett. 42, 5206–5211.
Miyagi, L., Kunz, M., Knight, J., Nasiatka, J., Voltolini, M., Wenk, H.R., 2008. In situ phase transformation and deformation of iron at high pressure and temperature. J. Appl. Phys. 104.
Miyagi, L., Merkel, S., Yagi, T., Sata, N., Ohishi, Y., Wenk, H.-R., 2009. Diamond anvil cell deformation of CaSiO3 perovskite up to 49GPa. Phys. Earth Planet. Inter. 174, 159–164.
Mookherjee, M., 2011. Elasticity and anisotropy of Fe3C at high pressures, 96, 1530–1536.
Mookherjee, M., Nakajima, Y., Steinle-Neumann, G., Glazyrin, K., Wu, X., Dubrovinsky, L., McCammon, C., Chumakov, A., 2011. High-pressure behavior of iron carbide (Fe7C3) at inner core conditions. J. Geophys. Res. Solid Earth 116, 1–13.
Mysen, B., 2019. Nitrogen in the earth: abundance and transport. Prog. Earth Planet. Sci. 6, 38.
Perreault, C., Huston, L.Q., Burrage, K., Couper, S.C., Miyagi, L., Moss, E.K., Pigott, J.S., Smith, J.S., Velisavljevic, N., Vohra, Y., et al., 2022. Strength of tantalum to 276 GPa determined by two x-ray diffraction techniques using diamond anvil cells. J. Appl. Phys. 131, 15905.
Ping, Y., Coppari, F., Hicks, D.G., Yaakobi, B., Fratanduono, D.E., Hamel, S., Eggert, J.H., Rygg, J.R., Smith, R.F., Swift, D.C., et al., 2013. Solid Iron compressed up to 560 GPa. Phys. Rev. Lett. 111, 65501.
Poirier, J.P., 1994. Light elements in the Earth's outer core: a critical review. Phys. Earth Planet. Inter. 85, 319–337.
Prescher, C., Dubrovinsky, L., Bykova, E., Kupenko, I., Glazyrin, K., Kantor, A., Mccammon, C., Mookherjee, M., Nakajima, Y., Miyajima, N., et al., 2015. High Poisson's ratio of Earth's inner core explained by carbon alloying. Nat. Geosci. 8, 220–223.
Reagan, M.M., Gleason, A.E., Liu, J., Krawczynski, M.J., Van Orman, J.A., Mao, W.L., 2018. The effect of nickel on the strength of iron nickel alloys: implications for the Earth's inner core. Phys. Earth Planet. Inter. 283, 43–47.
Romanowicz, B., Wenk, H.-R., 2017. Anisotropy in the deep earth. Phys. Earth Planet. Inter. 269, 58–90.
Rubin, A.E., Ma, C., 2017. Meteoritic minerals and their origins. Chem. Erde 77, 325–385.
Rueff, J.P., Krisch, M., Cai, Y.Q., Kaprolat, A., Hanfland, M., Lorenzen, M., Masciovecchio, C., Verbeni, R., Sette, F., 1999. Magnetic and structural alpha-epsilon phase transition in Fe monitored by x-ray emission spectroscopy. Phys. Rev. B 60, 14510–14512.
Sagatov, N., Gavryushkin, P.N., Inerbaev, T.M., Litasov, K.D., 2019. New high-pressure phases of Fe 7 N 3 and Fe 7 C 3 stable at Earth's core conditions: evidences for carbon-nitrogen isomorphism in Fe-compounds. RSC Adv. 9, 3577–3581.
Shen, G., Wang, Y., Dewaele, A., Wu, C., Fratanduono, D.E., Eggert, J., Klotz, S., Dziubek, K.F., Loubeyre, P., Fat'yanov, O.V., et al., 2020. Toward an international practical pressure scale: a proposal for an IPPS ruby gauge (IPPS-Ruby2020). High Pressure Res. 40, 299–314.
Shieh, S.R., Duffy, T.S., Shen, G., 2004. Elasticity and strength of calcium silicate perovskite at lower mantle pressures. Phys. Earth Planet. Inter. 143–144, 93–105.
Singh, A.K., Mao, H.K., Shu, J., Hemley, R.J., 1998. Estimation of single-crystal elastic moduli from polycrystalline x-ray diffraction at high pressure: application to feo and iron. Phys. Rev. Lett. 80, 2157–2160.
Smith, D.E., Zuber, M.T., Phillips, R.J., Solomon, S.C., Hauck, S.A., Lemoine, F.G., Mazarico, E., Neumann, G.A., Peale, S.J., Margot, J.-L., et al., 2012. Gravity field and internal structure of mercury from MESSENGER. Science 336, 214–217.
Söderlind, P., Moriarty, J.A., Wills, J.M., 1996. First-principles theory of iron up to earth-core pressures: structural, vibrational, and elastic properties. Phys. Rev. B 53, 14063–14072.
Speelmanns, I.M., Schmidt, M.W., Liebske, C., 2019. The almost lithophile character of nitrogen during core formation. Earth Planet. Sci. Lett. 510, 186–197.
Stähler, S.C., Khan, A., Banerdt, W.B., Lognonné, P., Giardini, D., Ceylan, S., Drilleau, M., Duran, A.C., Garcia, R.F., Huang, Q., et al., 2021. Seismic detection of the martian core. Science 373, 443–448.
Steenstra, E.S., van Westrenen, W., 2018. A synthesis of geochemical constraints on the inventory of light elements in the core of Mars. Icarus 315, 69–78.
Steenstra, E.S., Lin, Y., Rai, N., Jansen, M., van Westrenen, W., 2017. Carbon as the dominant light element in the lunar core, 102, 92–97.
Steinle-Neumann, G., Stixrude, L., Cohen, R.E., 1999. First-principles elastic constants for the hcp transition metals Fe, Co, and Re at high pressure. Phys. Rev. B 60, 791–799.
Sugiura, N., 1998. Ion probe measurements of carbon and nitrogen in iron meteorites. Meteorit. Planet. Sci. 33, 393–409.
Sumita, I., Bergman, M.I., 2007. In: G.B.T.-T. on, Schubert, G. (Eds.), 8.10 - Inner-Core Dynamics. Elsevier, Amsterdam, pp. 299–318.
Thompson, E.C., Davis, A.H., Bi, W., Zhao, J., Alp, E.E., Zhang, D., Greenberg, E., Prakapenka, V.B., Campbell, A.J., 2018. High-pressure geophysical properties of Fcc phase FeHX. Geochem. Geophys. Geosyst. 19, 305–314.
Trønnes, R.G., Baron, M.A., Eigenmann, K.R., Guren, M.G., Heyn, B.H., Løken, A., Mohn, C.E., 2019. Core formation, mantle differentiation and core-mantle interaction within earth and the terrestrial planets. Tectonophysics 760, 165–198.
Uts, I., Glazyrin, K., Lee, K.K.M., 2013. Effect of laser annealing of pressure gradients in a diamond-anvil cell using common solid pressure media. Rev. Sci. Instrum. 84, 103904.
Vander Kaaden, K.E., McCubbin, F.M., Turner, A.A., Ross, D.K., 2020. Constraints on the abundances of carbon and silicon in Mercury's Core from experiments in the Fe-Si-C system. J. Geophys. Res.: Planets 125, e2019JE006239.
Vasin, R.N., Kunz, M., Wenk, H.-R., Zepeda-Alarcon, E., 2023. Crystallographic texture formation in Fe-9wt%Si alloy during deformation and phase transition at high pressure. Geophys. J. Int. 234, 790–806.
Weber, R.C., Lin, P.-Y., Garnero, E.J., Williams, Q., Lognonné, P., 2011. Seismic detection of the lunar core. Science 331, 309–312.
Wenk, H.-R., Lutterotti, L., Kaercher, P., Kanitpanyacharoen, W., Miyagi, L., Vasin, R., 2014. Rietveld texture analysis from synchrotron diffraction images. II. Complex multiphase materials and diamond anvil cell experiments. Powder Diffract. 29, 220–232.
Wetzel, M.H., Rabending, T.T., Friák, M., Všianská, M., Šob, M., Leineweber, A., 2021. Phase stability of iron nitride Fe4N at high pressure—pressure-dependent evolution of phase equilibria in the Fe–N system. Materials 14, 3963–3990.
Yang, J., Sun, H., Chen, C., 2009. Anomalous strength anisotropy of γ'-Fe4N identified by first-principles calculations. Appl. Phys. Lett. 94, 151914.
Yoshizaki, T., McDonough, W.F., 2020. The composition of Mars. Geochim. Cosmochim. Acta 273, 137–162.
Zhao, C., Xu, L., Gui, W., Liu, J., 2020. Phase stability and vibrational properties of Iron-bearing carbonates at high pressure. Minerals 10, 1142–1156.